

1
2
3
4
5
6
7
8
9
10
11
12
13
14
15
16
17
18
19
20
21
22
23
24
25
26

This manuscript is a preprint version and has been submitted for publication in the Bulletin of the Seismological Society of America. Please note that, despite having undergone peer-review, the manuscript has yet to be formally accepted for publication. Subsequent versions of this manuscript may have slightly different content. If accepted, the final version of this manuscript will be available via the 'Peer-reviewed Publication DOI' link on the right-hand side of this webpage. Please feel free to contact any of the authors; we welcome feedback.

27 **Characterizing seismic scattering in 3D heterogeneous Earth by a single parameter**

28 Jagdish Chandra Vyas¹, Martin Galis^{2,3} and Paul Martin Mai¹

29 ¹*King Abdullah University of Science and Technology,*

30 ²*Faculty of Mathematics, Physics and Informatics, Comenius University, Bratislava, Slovakia ,*

31 ³*Earth Science Institute, Slovak Academy of Sciences, Bratislava, Slovakia*

32 *Email: Jagdish.Vyas@kaust.edu.sa*

33

34 **Abstract**

35 We derive a theoretical parameter for three seismic scattering regimes where seismic
36 wavelengths are either much shorter, similar, or much longer than the correlation length of small-scale
37 Earth heterogeneities. We focus our analysis on the power spectral density of the von Karman
38 autocorrelation function, used to characterize the spatial heterogeneity of small-scale variations of elastic
39 rock parameters that cause elastic seismic wave scattering. Our theoretical findings are verified by
40 numerical simulations. We discover 1) that seismic scattering is proportional to the standard deviation of
41 velocity variations in all three regimes, 2) that scattering is inversely proportional to the correlation length
42 for the regime where seismic wavelengths are shorter than correlation length, but directly proportional
43 to the correlation length in the other two regimes, and 3) that scattering effects are weak due to
44 heterogeneities characterized by a gentle decay of the von Karman autocorrelation function for regimes
45 where seismic wavelengths are similar or much longer than the correlation length.

46

47

48

49 Introduction

50 Heterogeneities in the Earth's crust and upper mantle cause seismic wave scattering, manifested
51 in so-called seismic coda waves that trail the main seismic phases. Often, coda waves are prominent
52 features of seismic recordings; they decay slowly with time, whereby the statistics of the temporal decay
53 provide information about the scattering process and the medium through which the waves travelled (e.g.
54 Aki 1969; Ritter et al., 1997; Sato and Fehler, 1998; Sato et al., 2012; Imperatori and Mai, 2013, 2015).
55 After Aki's (1969) interpretation that coda waves are back-scattered energy from uniformly distributed
56 heterogeneities in the Earth, several theoretical models were presented to explain seismic scattering, like
57 the single scattering model, the multiple scattering model, the diffusion model, or the energy-flux model
58 (Aki and Chouet, 1975; Sato, 1977; Gao et al., 1983; Frankel and Wennerberg, 1987). Additionally, the
59 coda envelope broadens with increasing travel distance due to wavefield scattering (Sato 2016), a process
60 that can be modelled employing a Markov approximation as stochastic treatment of the wave equation
61 in random media (Sato et al., 2012; Sato 2016). In contrast, S-wave coda excitation is mainly dominated
62 by scattering of direct S-waves from random heterogeneities in the Earth which can be modeled applying
63 the Born approximation (Sato et al., 2012; Sato and Emoto, 2017). In summary, coda waves are seismic-
64 wave energy trapped in the Earth due to the small-scale heterogeneities in the Earth.

65 Small-scale heterogeneities in the Earth can be described by a random spatial field superimposed
66 onto a background homogeneous medium. For this purpose, several random-field models have been
67 proposed; these are conveniently characterized by an autocorrelation function (ACF). For example, von
68 Karman, Gaussian, exponential and Henyey–Greenstein ACF or a fractal distribution are used to describe
69 random fields of seismic wave velocity variations in the Earth (e.g. Frankel and Clayton, 1986; Holliger and
70 Levander, 1992; Sato and Fehler, 1998; Sato, 2019). Most commonly, the von Karman ACF is used (e.g.

71 Hartzell et al. 2010; Imperatori and Mai, 2013; Bydlon and Dunham, 2015). The power spectral density
72 (PSD) of the von Karman AFC in three-dimension (3D) is given by

$$73 \quad p(k_m) = \frac{\sigma^2 (2\sqrt{\pi}a)^3 \Gamma(H + 1.5)}{\Gamma(H) (1 + k_m^2 a^2)^{(H+1.5)}}, \quad (1)$$

74 where a , H , σ and Γ are correlation length, Hurst exponent, standard deviation and the Gamma function,
75 respectively. We denote the wavenumber ($2\pi/\text{wavelength}$) of medium heterogeneity by k_m , and of the
76 seismic wavefield by k_w , and write wavenumber k in case k_m and k_w can be used interchangeably.

77 Several studies examined the range for correlation lengths, standard deviation, and Hurst
78 exponent in the Earth, both in observational studies and numerical simulations. Frankel and Clayton
79 (1986) reported that velocity fluctuations with standard deviation of 5% and correlation lengths of 10 km
80 (or greater) for 2D random media explain coda waves from micro earthquakes and travel time anomalies
81 across seismic arrays. Holliger (1996) obtained correlation lengths of 10 to 100 meters and Hurst exponent
82 in the range of 0.1 – 0.2 by analyzing sonic logs. Ritter et al. (1998) estimated wave-velocity perturbations
83 of 3 – 7% and correlation length of 1 – 16 km for the lithosphere in central France. Recently, Sato (2019)
84 reported that velocity perturbations are 1 – 10% in the Earth’s crust and upper mantle and that the Hurst
85 exponent typically falls in the range 0.0 – 0.5, while correlation lengths vary widely depending on sample
86 size or dimension of the measurement system. Overall, standard deviation, Hurst exponent, and
87 correlation lengths are found to be in the range of 1 – 10%, 0.0 – 0.5, and 1 – 15 km, respectively.

88 Seismic wave scattering occurs as the elastic waves encounter spatial variations of elastic medium
89 properties. Whilst even the deterministic reflection of a seismic wave at an internal interface of a seismic
90 velocity contrast could be classified as “seismic scattering”, the common nomenclature is that seismic
91 scattering is due to elastic-wave interactions with a spatially heterogeneous medium. In this context, the
92 (statistical) characteristics of the scattered wavefield depend on the stochastic properties of the medium.

93 This concept is conveniently described considering the wavelengths (λ) or wavenumbers (k_w) of the elastic
94 wave, and characteristic scales (wavelengths) of the random media.

95 Based on wavelength λ or wavenumber k_w of the seismic wave, and the correlation length a of
96 the random media, seismic wave scattering can be classified into three regimes: (i) $k_w a \gg 1$ ($\lambda \ll a$); (ii)
97 $k_w a \approx 1$ ($\lambda \approx a$); (iii) $k_w a \ll 1$ ($\lambda \gg a$) (Sato and Fehler, 1998; Sato et al., 2012;). The regime $k_w a \gg 1$
98 characterizes high-frequency scattering in which seismic wavelengths are much shorter than correlation
99 lengths. This regime is important for the earthquake engineering community in the context of high-
100 frequency (10 – 20 Hz) ground-shaking estimation, because seismic scattering redistributes seismic wave
101 energy (i.e. ground-motion amplitudes) in space and time. The regime $k_w a \approx 1$ represents the diffraction
102 condition, the most fundamental type of scattering. Finally, the regime $k_w a \ll 1$ denotes low-frequency
103 scattering for which seismic wavelengths are much longer than the correlation length of the random
104 medium. This regime is important for global seismology which uses primarily long wavelengths (0.01 – 0.5
105 Hz) to invert for the deterministic velocity structure of the Earth or earthquake source parameters (e.g.
106 centroid moment tensors).

107 Numerical and theoretical studies investigating the effects of seismic scattering on earthquake
108 ground-shaking suggest strong attenuation of ground-motion due to wavefield scattering (Shapiro and
109 Kneib, 1993; Mai, 2009; Hartzell et al., 2010; Imperatori and Mai, 2012, 2013; Yoshimoto et al., 2015; Vyas
110 et al., 2018). Bydlon and Dunham (2015) explained theoretically how the parameters describing the von
111 Karman ACF control wavefield scattering in 2D. Using numerical simulations, they verified that a
112 parameter $\rho_0 = \sigma/a^H$ determines the nature of scattering in the $k_w a \gg 1$ limit, regardless of the specific
113 values of σ and a . However, how the other parameters of the von Karman ACF (a , σ and H) affect 3D
114 seismic scattering has not been explored yet in detail.

115 Here, we investigate seismic wave scattering in 3D and verify our theoretical results by numerical
116 simulations. First, we examine the mathematical expression for the power spectral density (PSD) of the
117 von Karman AFC (Eq. 1) to identify parameters that represent scattering behaviour in 3D for the three
118 different regimes, $k_w a \gg 1$, $k_w a \approx 1$ and $k_w a \ll 1$. Then we test our theoretical findings through numerical
119 simulations that cover the parameter space of these three regimes and allow us to examine how
120 scattering manifests itself in seismic waveforms and ground-motion amplitudes.

121

122 Theory

123 Bydlon and Dunham (2015) investigated high-frequency scattering ($f = 1 - 30$ Hz) by considering
124 a 2D problem and the regime $k_w a \gg 1$. To analyze scattering under these assumptions, they simplified
125 the PSD of the von Karman ACF to obtain the root-mean-square (RMS) fluctuations of normalized seismic
126 wave velocity (wave speed), and then derived which parameters (i.e., a , H and/or σ) control wavefield
127 scattering. Here, we extend their approach to 3D by considering three different $k_w a$ regimes.

128 Wavefield scattering is strongest if the wavenumber of the seismic wave is comparable to the
129 wavenumber of heterogeneities in the medium. Hence, we simplify the PSD for the three regimes ($k_w a$
130 $\gg 1$, $k_w a \approx 1$ and $k_w a \ll 1$) under the diffraction condition to obtain RMS of fluctuations of normalized
131 wave velocity (computed as the square root of the mean power, denoted as P_{RM}). By assuming the
132 diffraction condition, we derive theoretically the parameter P_{RM} , which in fact dictates the wavefield
133 scattering in 3D. Seismic scattering associated with a particular seismic wavelength will depend on the
134 amplitudes of velocity variations corresponding to that wavelength. However, we aim to understand the
135 overall wavefield scattering behaviour for a range of seismic wavelengths and heterogeneity scales in the
136 medium. Therefore, our P_{RM} derivations are not only applicable for a monochromatic source or a single-
137 wavelength medium, but instead capture the broadband nature of scattering. Note that we only

138 summarize the final equations for P_{RM} for each regime in the main text; further details of the derivations
 139 are provide in the Electronic supplement.

140

141 **Regime I: $k_w a \gg 1$**

142 Our P_{RM} derivation for this regime assumes that the source excites waves of equal amplitude (a
 143 flat source spectrum) with wavenumbers from k_{min} to infinity, all of which interact with heterogeneities in
 144 the medium with the same range of wavenumbers (albeit at different “intensity” or strength). Note that
 145 this assumption is not completely satisfied in nature as earthquakes typically excite only a limited range
 146 of frequencies, and not all of these frequencies will interact with the generally scale-limited medium
 147 heterogeneities. However, the assumption allows us to calculate the overall wavefield scattering
 148 behaviour for the regime $k_w a \gg 1$, for which seismic wavelengths are much shorter than the correlation
 149 length of small-scale Earth heterogeneities. Then, the RMS fluctuations of normalized wave velocity (P_{RM})
 150 can be approximated by

151
$$P_{RM} = \sqrt{\frac{1}{4\pi} \int_{k_{min}}^{\infty} p(k) k^2 dk} \approx \sqrt{(c_0 + c_1 H + c_2 H^2)} \frac{\sigma}{a^H} \frac{\pi^{1/4}}{k_{min}^H} \quad (2)$$

152 Therefore, the P_{RM} dependency is given by,

153
$$P_{RM} \propto \sqrt{(c_0 + c_1 H + c_2 H^2)} \frac{\sigma}{a^H}, \quad (3)$$

154 where we approximate the term depending on H by a quadratic function (with coefficients $c_0= 0.89$, $c_1=$
 155 0.53 , and $c_2= -0.08$; see Fig. S1a and derivation in electronic supplement for details). Note that we
 156 characterize the scattering behavior for the entire regime $k_w a \gg 1$, rather than for a particular wavelength
 157 in this regime by using integration limits in Eq. 2 from k_{min} to infinity, and not over any arbitrary
 158 wavenumber range. Therefore, the parameter P_{RM} (Eq. 3) becomes independent of wavenumber.

159 Comparing Eq. 3 with parameter $p_0 = \sigma/a^H$ (Bydlon and Dunham, 2015) reveals that even in the regime
 160 $k_w a \gg 1$, scattering in 3D is more complex than in 2D. Eq. 3 illustrates that in the high-frequency scattering
 161 regime, (a) scattering is proportional to the standard deviation of the velocity fluctuations, (b) scattering
 162 is inversely proportional to the correlation length a , and c) the Hurst exponent has a strongly non-linear
 163 effect on scattering. Interestingly, if the Hurst exponent approaches its theoretical lower limit of zero
 164 ($H \rightarrow 0$), Eq. 3 can be further simplified to

$$165 \quad P_{RM} \propto \sigma, \quad (4)$$

166 indicating that scattering is controlled by the standard deviation of the velocity variations in this case.

167

168 **Regime II: $k_w a \approx 1$**

169 We assume that the source excites waves having a flat source spectrum with wavenumbers from
 170 k_1 to k_2 , all of which interact with medium heterogeneities of the same wavenumber range. If seismic
 171 wavelengths are comparable to the correlation length of heterogeneities, the RMS fluctuations of
 172 normalized wave velocity can be approximated by

$$173 \quad P_{RM} = \sqrt{\frac{1}{4\pi} \int_{k_1}^{k_2} p(k) k^2 dk} \approx \left(\frac{\pi}{18}\right)^{1/4} a^{3/2} \sigma \sqrt{(c_1 H + c_2 H^2)} \sqrt{(k_2^3 - k_1^3)} \quad (5)$$

174 Therefore, the P_{RM} dependency is given by,

$$175 \quad P_{RM} \propto \sqrt{(c_1 H + c_2 H^2)} a^{3/2} \sigma, \quad (6)$$

176 Where coefficients are given as $c_1 = 0.93$, and $c_2 = -0.27$ (see Fig. S1b). Analyzing Eq.6 for P_{RM} reveals that
 177 a) scattering is proportional to σ , similar to the regime $k_w a \gg 1$, b) scattering is proportional to correlation
 178 length a , in contrast to regime $k_w a \gg 1$ (compare Eq. 6 with Eq. 3), and c) scattering is correlated with the
 179 Hurst exponent (as H approaches zero, scattering effects weaken and become eventually negligible).

180

181 **Regime III: $k_w a \ll 1$**

182 Here, we assume that the source excites waves of equal amplitude (a flat source spectrum) with
183 wavenumbers from zero to k_1 , all of which interact with medium heterogeneities. If seismic wavelengths
184 are much longer than the correlation length of the heterogeneities, the RMS fluctuations of normalized
185 wave velocity can be approximated by

186
$$P_{RM} = \sqrt{\frac{1}{4\pi} \int_0^{k_1} p(k) k^2 dk} \approx \left(\frac{4\pi}{9}\right)^{1/4} a^{3/2} \sigma \sqrt{(c_1 H + c_2 H^2)} k_1^{3/2} \quad (7)$$

187 Therefore, the P_{RM} dependency is given by

188
$$P_{RM} \propto \sqrt{(c_1 H + c_2 H^2)} a^{3/2} \sigma, \quad (8)$$

189 where coefficients $c_1 = 0.93$, and $c_2 = 0.40$ (see Fig. S1c). Note that only constant c_2 is different between
190 Eq. 8 and Eq. 6, therefore, P_{RM} for the regime $k_w a \ll 1$ is similar to that for $k_w a \approx 1$, except that the effect
191 of H on scattering is stronger for $k_w a \ll 1$ than for $k_w a \approx 1$ because $c_2 > 0$ (compare Eq. 6 and Eq. 8).

192

193 **Verification of Theory by Simulations**

194 In this section, we verify our findings (Eq. 3, 4, 6, 8) by conducting seismic wavefield simulations
195 in random media. Since our simulations do not strictly satisfy the assumptions used for the derivations of
196 P_{RM} , we validate only proportionality or inverse-proportionality of P_{RM} with correlation length, standard
197 deviation, and Hurst exponent, rather than the complete expressions (Eq. 3, 4, 6, 8). To numerically test
198 our results for the three scattering regimes, we fix the correlation length a and modify the source
199 frequency to radiate seismic waves with different frequencies (i.e., we are altering the wavenumber k_w).
200 For computing synthetic seismograms, we use a generalized 3D finite-difference method with second-

201 order accuracy in space and time (SORD code by Ely et al., 2008). Our simulations consider several
202 discretized Earth models, a point-source earthquake model, and receiver locations at which ground-
203 motions are stored. We then analyze waveforms and peak ground acceleration (PGA), and confront the
204 numerical results with our theoretical analysis.

205

206 ***Set up for Numerical Modeling***

207 We consider a point source (moment magnitude $M_w \sim 2.84$) at a depth of 7.5 km, with strike, dip,
208 and rake of 22.5° , 90° , and 0° , respectively. The source-time function (STF) is a Gaussian. We define STFs
209 to radiate frequencies required to properly sample the three regimes ($f_{max} = 5.0$ Hz for $k_w \cdot a \gg 1$, $f_{max} = 0.5$
210 Hz for $k_w \cdot a \approx 1$ and $f_{max} = 0.03$ Hz for $k_w \cdot a \ll 1$, see Fig S2; f_{max} is the high frequency limit of the flat portion
211 of the slip velocity spectrum). For example, a point source radiating frequencies of 5.0 Hz, 0.5 Hz and 0.03
212 Hz in a heterogeneous medium with background shear-wave velocity 3.464 km/s and stochastic
213 perturbations with correlation length of 1 km yields $k_w \cdot a \approx 9.0$, 0.9 and 0.05, respectively.

214 To create a velocity model with small-scale heterogeneities, we add random-field variations of
215 seismic wave velocities, characterized by an isotropic von Karman ACF, to the uniform background Earth
216 model (with S-wave velocity 3464 m/s, P-wave velocity, 6000 m/s, and density 2700 kg/m^3). In total, we
217 generate twelve 3D computational models (M1 to M12; Table 1), considering three correlation lengths
218 (1.0 km, 5.0 km, 10.0 km), two values of standard deviation (5%, 10%), and two Hurst exponents (0.1, 0.5).
219 For each combination of medium parameters, we create one realization of random inhomogeneity in S-
220 wave speed, P-wave speed, and density. S-wave velocity distributions at the surface are shown for all
221 twelve computational models (Figs 1a, 1b). Theoretical 1D power spectra for seven selected models are
222 plotted to illustrate effects of correlation lengths, standard deviation, and Hurst exponent on the spectral

223 shape (Fig 1c). Power spectra for two specific models, M2 and M11, are examined for the three scattering
224 regimes considering the three STFs used in this study (Fig. 1d).

225 The size of the computational domain must be chosen such that seismic waves propagate to large-
226 enough distances that ensure sufficient wave interaction with medium heterogeneities to develop
227 scattering. At the same time, the domain should be as small as possible to minimize computational cost.
228 Given these constraints, we define different computational domain sizes and grid spacings, depending on
229 scattering regime. For the regime $k_w a \gg 1$, we use grid spacing $h=25\text{m}$ ($dt=0.0015\text{ s}$) on a domain of
230 $60 \times 60 \times 15\text{ km}$, allowing travel distance of ~ 40 wavelengths (at $f = 5.0\text{ Hz}$). Combining these models with
231 STF1 (Fig. S2a) yields $k_w a$ in the range of 9 to 90. For $k_w a \approx 1$ we use $h=75\text{m}$ ($dt=0.0045\text{ s}$) and a larger
232 domain, $355 \times 355 \times 30\text{ km}$, corresponding to travel distance of ~ 50 wavelengths (at $f = 0.5\text{ Hz}$). The eight
233 corresponding models are denoted by the suffix “-L” (see Tab 1 and Fig S3) and when combined with STF2
234 (Fig. S2b), they result in $k_w a$ -values between 0.9 and 4.5. For $k_w a \ll 1$, we use $h=1000\text{m}$ ($dt=0.055\text{ s}$) and
235 an extra-large domain, $2000 \times 2000 \times 60\text{ km}$ (ignoring the spherical nature of Earth), denoted by the suffix
236 “-EL” (see Tab 1 and Fig S4). When combined with STF3 (Fig. S2c), the corresponding $k_w a$ values fall in the
237 range 0.27 to 0.5. Owing to the very long wavelengths in this regime ($\sim 115\text{km}$ at $f = 0.03\text{ Hz}$), the domain
238 allows travel distances of only ~ 15 wavelengths, significantly lower than those in the two previous
239 regimes. However, the cost for computational models allowing travel distances of $\sim 45\text{-}50$ wavelengths
240 would be exorbitant. In total, we use 28 computational models with random inhomogeneities, twelve of
241 which are for $k_w a \gg 1$, eight for $k_w a \approx 1$ and eight for $k_w a \ll 1$ regimes. Our simulations consumed nearly
242 four million core-hours of computational resources on a Cray XC40 supercomputer. To establish a base
243 case for comparison, we also conduct simulations in a homogeneous medium for each regime.

244 We store synthetic seismograms at receivers placed in a concentric rings for $k_w a \gg 1$, but for $k_w a$
245 ≈ 1 and $k_w a \ll 1$ we consider only a one quadrant to save computational costs (Fig 1a, Fig S3a, Fig S4a).
246 The epicenter is placed in the center of the simulation domain for $k_w a \gg 1$, but for $k_w a \approx 1$ and $k_w a \ll 1$

247 it is in the lower left corner. Receiver geometry and epicenter location are designed to obtain the best
248 possible azimuthal coverage of stations and to allow for sufficiently large travel distances for seismic
249 waves to develop scattering, at the same time also minimizing computational costs. Virtual stations are
250 distributed along rings with radial spacing of 0.1, 0.2 and 3.5 km, for $k_w a \gg 1$, $k_w a \approx 1$ and $k_w a \ll 1$
251 regimes, respectively. Therefore, each ring (arc) of stations contains a different number of stations at
252 different azimuths. The smallest ring (arc) used for PGA statistics has 314 (radius 5km), 196 (radius 25 km)
253 and 134 (radius 300 km) stations for the three regimes ($k_w a \gg 1$; $k_w a \approx 1$; $k_w a \ll 1$). Therefore, our
254 receiver geometry is statistically independent and PGA statistics are robust. All waveforms are low-pass
255 filtered using a fourth-order Butterworth filter with cutoff frequencies of 5 Hz, 0.5 Hz and 0.03 Hz for the
256 three scattering regimes, respectively.

257

258 ***Quantifying Seismic Scattering in Numerical Results***

259 Seismic scattering redistributes energy in space and time from direct P- and S-waves into the late-
260 arriving coda waves. Consequently, peak ground acceleration (PGA) in a homogeneous medium will be,
261 on average, higher than in a scattering medium. Therefore, we examine ratios of PGA-values to quantify
262 scattering “strength” in numerical simulations. Horizontal components of acceleration are mostly used in
263 earthquake engineering applications (e.g., Boore and Atkinson, 2008; Chiou and Youngs, 2008), because
264 wave amplitudes on the vertical component are usually smaller than on the horizontal components.
265 Therefore, we analyze horizontal PGA (computed as maximum magnitude of acceleration from the two
266 horizontal components). We illustrate scattering effects and resulting PGA values by comparing
267 waveforms for selected receivers s1, s2 and s3 (see Fig 1a for their locations).

268 In Fig 2 we compare horizontal-component ground-acceleration waveforms at selected stations
269 for the regime $k_w a \gg 1$. Fig 2a compares waveforms and PGA values for two values of standard deviation

270 (models M3 and M6) with those for the homogeneous medium PGA values are consistent with our
271 expectation that stronger scattering leads to lower PGA. In this particular case, the scattering for model
272 M3 is weaker than for model M6 (see also acceleration snapshots in Fig S5). Additionally, ground
273 acceleration comparison for M6 at three stations (Fig S6) shows prominent coda evolution and reduced
274 maximum acceleration values as epicentral distance increases (from s_4 to s_6). Fig 2b reveals that
275 waveforms for two models with different correlation lengths (M1 and M3) are almost identical, with only
276 small time shifts. This indicates that the two models yield almost identical levels of scattering (confirmed
277 also by comparing acceleration snapshots for M1 and M3 in Fig S5). Correspondingly, PGA values are
278 comparable. In addition, these comparisons (Figs 2a and 2b) suggest that scattering is primarily controlled
279 by the standard deviation of the medium heterogeneities, whereas the correlation length has a negligible
280 effect for a small H value ($H = 0.1$), consistent with our theoretical analysis in Eq. 4. However, we note that
281 PGA only works well in such comparisons because we computed a reference solution for the
282 homogeneous medium. Without such a reference case, interpreting PGA values directly as indicator for
283 “scattering strength” would be misleading.

284

285 ***Statistical Analysis of Scattering***

286 Next, we calculate the mean and standard deviation of PGA values for all stations at a given
287 epicentral distance and for a given computational model (see Fig. S7 for a comparative summary of all
288 computational models). To estimate the average scattering-related PGA reduction at a given epicentral
289 distance, we define the “mean PGA ratio” (MPR), at a particular epicentral distance, as the ratio between
290 the mean PGA values from any heterogeneous Earth model to the mean PGA-values from the reference
291 homogeneous Earth model. As epicentral distance increases, the MPR is expected to decrease because
292 the redistribution of seismic energy due to scattering is cumulative with propagation distance.

293 Figure 3 summarizes our results for $k_w a \gg 1$. For $H = 0.1$ we find the MPRs for models with $\sigma =$
 294 10% (M4, M5, M6) are lower than for models with $\sigma = 5\%$ (M1, M2, M3) (Fig. 3a). At the same time, MPRs
 295 of both groups are very similar, supporting our theoretical conclusion that for small H the correlation
 296 length has insignificant effects on scattering, which in this regime is controlled by standard deviation (Eq.
 297 4). The apparent plateau in MPRs for distances 10 to 20 km is a consequence of source effects being
 298 masked by wavefield scattering effects due to the hypocenter location (see Fig. S8 for more details on the
 299 effects of hypocentral depths on MPRs). Fig 3b compares solutions for $H=0.5$, for which we expect a
 300 significant effect of both correlation length and standard deviation. For fixed σ , we observe that the MPR's
 301 for models with shorter correlation length are lower than those with longer correlation length ($MPR_{M7} <$
 302 $MPR_{M8} < MPR_{M9}$; similarly $MPR_{M10} < MPR_{M11} < MPR_{M12}$). This finding is consistent with our conclusion
 303 that scattering is inversely proportional to correlation length for large H (Eq. 3). Also, MPR's for models
 304 with $\sigma = 10\%$ are lower than those for corresponding models with $\sigma = 5\%$ ($MPR_{M10} < MPR_{M7}$, $MPR_{M11} <$
 305 MPR_{M8} , $MPR_{M12} < MPR_{M9}$), demonstrating that scattering is proportional to the standard deviation of
 306 velocity variations for large H . Thus, these observations validate our theoretical conclusions for the regime
 307 $k_w a \gg 1$.

308 The MPR-analysis for regime $k_w a \approx 1$ is summarized in Figure 4. For both values of H , the MPR's
 309 for models with shorter correlation length are higher than MPR's for models with longer correlation length
 310 ($MPR_{M1-L} > MPR_{M2-L}$, $MPR_{M4-L} > MPR_{M5-L}$, $MPR_{M7-L} > MPR_{M8-L}$, $MPR_{M10-L} > MPR_{M11-L}$),
 311 revealing that scattering is proportional to correlation length (see Fig. 4a and Fig. 4b). The MPR's for
 312 models with $\sigma = 5\%$ are higher than those for model with $\sigma = 10\%$ ($MPR_{M1-L} > MPR_{M4-L}$, $MPR_{M2-L} >$
 313 MPR_{M5-L} , $MPR_{M7-L} > MPR_{M10-L}$, $MPR_{M8-L} > MPR_{M11-L}$), indicating that scattering is proportional to
 314 the standard deviation of velocity fluctuations. The MPR's for models with $H = 0.1$ are larger than those
 315 for models with $H = 0.5$ ($MPR_{M1-L} > MPR_{M7-L}$, $MPR_{M2-L} > MPR_{M8-L}$, $MPR_{M4-L} > MPR_{M10-L}$,

316 $MPR_{M5-L} > MPR_{M11-L}$), therefore, scattering is proportional to the Hurst exponent H . These
317 observations are also consistent with our theoretical findings for $k_w a \approx 1$ (see Eq. 6).

318 Finally, we show MPR statistics for the regime $k_w a \ll 1$ (Figure 5). First, recall that due to
319 prohibitively large computational costs we used a smaller computational domain (see Section *Set up for*
320 *Numerical Modeling*). Consequently, scattering is less well developed for $k_w a \ll 1$, and hence effects on
321 MPR's are not as pronounced as in the other two regimes. Still, the effects are strong enough to support
322 our theoretical derivation (see waveform comparison in Fig. S9 and station locations in Fig. S4). The MPR's
323 for models with 10 km correlation length are lower than those for 5 km correlation length ($MPR_{M3-EL} <$
324 MPR_{M2-EL} , $MPR_{M6-EL} < MPR_{M5-EL}$, $MPR_{M9-EL} < MPR_{M8-EL}$, $MPR_{M12-EL} < MPR_{M11-EL}$), showing
325 that scattering is proportional to correlation length. The MPR's for models with $\sigma = 10\%$ are lower than
326 those for $\sigma = 5\%$ ($MPR_{M12-EL} < MPR_{M9-EL}$, $MPR_{M11-EL} < MPR_{M8-EL}$), suggesting that scattering is also
327 proportional to the standard deviation of velocity variations. These observations agree well with our
328 theoretical considerations for $k_w a \ll 1$ (see Eq. 8).

329 In summary, our results from numerical simulations are consistent with our conclusions based on
330 theoretical derivation for all three considered scattering regimes.

331

332 Discussion and Conclusions

333 We derive a new parameter P_{RM} to quantify 3D seismic wavefield scattering. P_{RM} is based on the
334 assumption that small-scale heterogeneities in seismic velocity are characterized by the von Karman ACF.
335 P_{RM} helps to understand the influence of the parameters of the von Karman ACF on seismic scattering for
336 three considered regimes ($k_w a \gg 1$, $k_w a \approx 1$ and $k_w a \ll 1$). We test our theoretical consideration through

337 statistical analysis of a suite of numerical simulations that capture seismic scattering in different scattering
338 regimes.

339 We find that the strength of wavefield scattering in all three regimes is proportional to the
340 standard deviation of heterogeneities. Seismic scattering is also proportional to the correlation length in
341 the regimes $k_w a \approx 1$ and $k_w a \ll 1$, but for the regime $k_w a \gg 1$ the scattering is inversely proportional to
342 correlation length. For regime $k_w a \gg 1$, we also find that if the Hurst exponent H approaches zero,
343 scattering will be controlled solely by standard deviation. However, for $k_w a \approx 1$ and $k_w a \ll 1$, scattering
344 is weakly impacted for small values of H , with scattering vanishing in the limit of $H \rightarrow 0$.

345 To further explain these findings, we integrate the PSD for the 3D problem (Eq. 1) with respect to
346 wavenumber k_m ,

$$347 \int_0^{\infty} p(k_m) dk_m = 4\pi^2 a^2 \sigma^2 H \quad (9)$$

348 Eq. 9 represents the area under the power spectrum for a three dimensional isotropic PSD along one
349 wavenumber axis; it reveals that the area under the power spectrum depends on a , H and σ , implying also
350 that the area under the power spectrum will be zero if any of a or H or σ is zero. For example, M2 has
351 larger area under the power spectrum than M1 due to larger correlation lengths of M2, although standard
352 deviation and Hurst exponent are identical for M1 and M2 (see Fig. 1c). The area under the power
353 spectrum can be linked to wavefield scattering as it represents the total scattering power of the
354 heterogeneous medium in terms of the sum of amplitude squares of seismic-velocities. Correspondingly,
355 in the limit of any of the von Karman parameters approaching zero, wavefield scattering will become
356 negligible.

357 Quantitative analysis of power spectra in Fig 1c helps to interpret the implications of Eq. 9 for the
358 three scattering regimes. Therefore, our theoretical findings, confirmed by numerical simulations, can be

359 explained by the amplitude and shape of the PSD. The standard deviation scales the power spectra
360 without changing the shape of the power spectra (hence, area under the power spectra), resulting in
361 scattering proportional to σ for all three regimes ($k_w a \gg 1$, $k_w a \approx 1$ and $k_w a \ll 1$). The tails of the power
362 spectra (decaying part) show inverse proportionality with correlation length a (e.g. compare tails of M7,
363 M8 and M9 in Fig 1c), thus resulting in scattering being inversely proportional to a for the regime $k_w a \gg$
364 1 . However, the plateau and corners (corner wavenumber = $2\pi/a$) of the power spectra scale with
365 correlation length, leading to scattering being proportional to correlation length for $k_w a \ll 1$ and $k_w a \approx$
366 1 , respectively (e.g. compare plateau and corners of M7, M8 and M9 in Fig 1c). Furthermore, the plateau
367 and corner of power spectra grow as H increases, therefore, scattering is proportional to H for $k_w a \ll 1$
368 and $k_w a \approx 1$. Fig 1c also shows that the tails of the power spectra tend to merge for small H (see M1, M2
369 and M3) and diverge as H increases (compare M7, M8 and M9), implying a more complex dependency on
370 H for scattering in the regime $k_w a \gg 1$. Hence, our findings can be explained by the shape and amplitude
371 of the PSD function of the von Karman ACF.

372 Comparing our results for $k_w a \gg 1$ for the 3D problem (Eq. 3) with the 2D results by Bydlon and
373 Dunham (2015) ($p_0 = \sigma/a^H$) reveals that the effect of standard deviation and correlation length remains
374 the same, but the effect of the Hurst exponent H is stronger in 3D. However, if the Hurst exponent
375 approaches zero, scattering effects are dominated by standard deviation, both in 2D and 3D. This is an
376 important finding, since values of H smaller than 0.5 have been reported by Sato (2019) for the Earth's
377 crust and mantle.

378 Here we propose to quantify the overall wavefield scattering directly via an integral of the PSD
379 function of the random media. We note that Sato et al. (2012) analyzed a plane wave scattered by a
380 localized inhomogeneity using the wave equation. They solved the wave equation utilizing Born
381 approximation, i.e., they assumed that the amplitude of velocity variations is negligibly small compared

382 to background velocity, that the amplitude of the scattered wavefield is negligibly small compared to the
 383 amplitude of incident wavefield, and that the scattered wavefield has only a small phase change after
 384 passing through the heterogeneity. Therefore, derivations by Sato et al., (2012) are valid for high
 385 frequency scattering, when seismic wavelengths are very short compared to the length scales of medium
 386 heterogeneity. They found that the scattering coefficient depends on the PSD function of the random
 387 media as follows (Eq. 4.25 from Sato et al., 2012),

$$388 \quad g(\theta, \omega) = \frac{k_w^4}{\pi} P(2k_w \sin \frac{\theta}{2}) \quad (10)$$

389 In Eq. 10, θ is the angle between incident and scattered waves; ω and k_w are angular frequency
 390 and wavenumber of the incident wavefield, respectively. The scattering coefficient reveals that a wave
 391 with wavenumber k_w interacts with medium heterogeneities with wavenumber k_m , leading to

$$392 \quad k_m = 2k_w \sin \frac{\theta}{2} = 2 \sin \frac{\theta}{2} k_w = C k_w \quad (11)$$

393 The scaling factor C is a function of the scattering angle θ and ranges from 0 to 2, for forward (θ
 394 = 0) and backward ($\theta = \pi$) scattering, respectively. The average value of C (over θ) indicates the overall
 395 interaction between k_m and k_w , averaged over all directions. The average value of C is 1.27, therefore k_m
 396 $\sim k_w$. This is consistent with our assumption for the derivation of P_{RM} , although we apply an ideal
 397 diffraction condition ($k_m = k_w$). Note that our P_{RM} results will not change even if we use a more relaxed
 398 diffraction condition (i.e. $k_m \sim k_w$). Hence, our theory complies with Sato et al. (2012), but taking a different
 399 perspective on evaluating the wavefield scattering. Note that the detailed theoretical analysis to fully
 400 describe the wavefield scattering in 3D requires considering the 3D elastic wave equation with complex
 401 earthquake source characteristics (radiated wavefield) in 3D random media with anisotropic wave
 402 propagation. This derivation is beyond the scope of the present study.

403 In summary, our theoretical analysis of the von Karman PSD, used to represent random spatial
404 variation in seismic wave velocities and rock density, helps to develop a physics-based understanding of
405 how standard deviation, correlation length, and Hurst exponent govern three-dimensional seismic
406 wavefield scattering for three scattering regimes ($k_w a \gg 1$, $k_w a \approx 1$ and $k_w a \ll 1$). This will help studies
407 on ground-motion simulations for earthquake shaking as well as research on global seismic wave
408 propagation in 3D Earth models to properly simulate elastic wavefield scattering.

409

410 **Data and Resources**

411 Ground-motions simulations carried out to verify the outcomes of theoretical derivation
412 generated nearly 2.5 TB of data which can be provided via personal communication. This manuscript has
413 an electronic supplement which comprises the complete derivation of the root-mean-square fluctuations
414 of normalized wave velocity using power spectral density of the von Karman autocorrelation function for
415 three scattering regimes ($k_w a \gg 1$, $k_w a \approx 1$ and $k_w a \ll 1$). The electronic supplement also contains figures
416 of the quadratic fit to ratios of gamma functions, three Gaussian source time functions, simulations setup
417 depicting receiver geometry and S-wave speed variations, acceleration waveforms comparison from few
418 receivers, snapshots of ground-acceleration wavefield at Earth surface and peak ground acceleration
419 statistics.

420

421 **Acknowledgements**

422 The research presented in this article is supported by King Abdullah University of Science and Technology
423 (KAUST) in Thuwal, Saudi Arabia, grants BAS/1/1339-01-01 and URF/1/3389-01-01. MG was partially
424 supported by Scientific Grant Agency VEGA, grant 2/0046/20. Earthquake ground-motion simulations

425 have been carried out using the KAUST Supercomputing Laboratory (KSL), and we acknowledge the
426 support of the KSL staff. We thank Art Frankel and an anonymous reviewer, as well as the editor Adrien
427 Oth, for their constructive critical review that helped us to improve the manuscript.

428

429 **References**

430 Aki, K. (1969). Analysis of the seismic coda of local earthquakes as scattered waves. *Journal of*
431 *geophysical research*, 74(2), 615-631.

432 Aki, K., & Chouet, B. (1975). Origin of coda waves: source, attenuation, and scattering effects.
433 *Journal of geophysical research*, 80(23), 3322-3342.

434 Boore, D. M., & Atkinson, G. M. (2008). Ground-motion prediction equations for the average
435 horizontal component of PGA, PGV, and 5%-damped PSA at spectral periods between 0.01 s and 10.0 s.
436 *Earthquake Spectra*, 24(1), 99-138.

437 Bydlon, S. A., & Dunham, E. M. (2015). Rupture dynamics and ground motions from earthquakes
438 in 2-D heterogeneous media. *Geophysical Research Letters*, 42(6), 1701-1709.

439 Chiou, B. J., & Youngs, R. R. (2008). An NGA model for the average horizontal component of peak
440 ground motion and response spectra. *Earthquake Spectra*, 24(1), 173-215.

441 Ely, G. P., Day, S. M., & Minster, J. B. (2008). A support-operator method for viscoelastic wave
442 modelling in 3-D heterogeneous media. *Geophysical Journal International*, 172(1), 331-344.

443 Frankel, A., & Clayton, R. W. (1986). Finite difference simulations of seismic scattering:
444 Implications for the propagation of short-period seismic waves in the crust and models of crustal
445 heterogeneity. *Journal of Geophysical Research: Solid Earth*, 91(B6), 6465-6489.

446 Frankel, A., & Wennerberg, L. (1987). Energy-flux model of seismic coda: separation of scattering
447 and intrinsic attenuation. *Bulletin of the Seismological Society of America*, 77(4), 1223-1251.

448 Gao, L. S., Biswas, N. N., Lee, L. C., & Aki, K. (1983). Effects of multiple scattering on coda waves in
449 three-dimensional medium. *pure and applied geophysics*, 121(1), 3-15.

450 Hartzell, S., Harmsen, S., & Frankel, A. (2010). Effects of 3D random correlated velocity
451 perturbations on predicted ground motions. *Bulletin of the Seismological Society of America*, 100(4),
452 1415-1426.

453 Holliger, K. (1996). Upper-crustal seismic velocity heterogeneity as derived from a variety of P-
454 wave sonic logs. *Geophysical Journal International*, 125(3), 813-829.

455 Holliger, K., & Levander, A. R. (1992). A stochastic view of lower crustal fabric based on evidence
456 from the Ivrea zone. *Geophysical Research Letters*, 19(11), 1153-1156.

457 Imperatori, W., & Mai, P. M. (2012). Sensitivity of broad-band ground-motion simulations to
458 earthquake source and Earth structure variations: an application to the Messina Straits (Italy). *Geophysical
459 Journal International*, 188(3), 1103-1116.

460 Imperatori, W., & Mai, P. M. (2013). Broad-band near-field ground motion simulations in 3-
461 dimensional scattering media. *Geophysical journal international*, 192(2), 725-744.

462 Imperatori, W., & Mai, P. M. (2015). The role of topography and lateral velocity heterogeneities
463 on near-source scattering and ground-motion variability. *Geophysical Journal International*, 202(3), 2163-
464 2181.

465 Mai, P. M. (2009). Ground Motion: Complexity and Scaling in the Near Field of Earthquake
466 Ruptures. *Encyclopedia of Complexity and System Sciences*, R. Meyers (Editor), Springer, ISBN 978-0-387-
467 69572-3, pp 4435–4474.

468 Ritter, J. R., Mai, P. M., Stoll, G., & Fuchs, K. (1997). Scattering of teleseismic waves in the lower
469 crust observations in the Massif Central, France. *Physics of the earth and planetary interiors*, 104(1-3),
470 127-146.

471 Ritter, J. R., Shapiro, S. A., & Schechinger, B. (1998). Scattering parameters of the lithosphere
472 below the Massif Central, France, from teleseismic wavefield records. *Geophysical Journal International*,
473 134(1), 187-198.

474 Sato H., & Fehler, M. C. (1998). *Seismic Wave Propagation and Scattering in the Heterogenous*
475 *Earth*, , Springer-Verlag, New York, ISBN #0-387-98329-5.

476 Sato, H. (1977). Single isotropic scattering model including wave conversions simple theoretical
477 model of the short period body wave propagation. *Journal of Physics of the Earth*, 25(2), 163-176.

478 Sato, H. (2016). Envelope broadening and scattering attenuation of a scalar wavelet in random
479 media having power-law spectra. *Geophysical Journal International*, 204(1), 386-398.

480 Sato, H. (2019). Power spectra of random heterogeneities in the solid earth. *Solid Earth*, 10(1),
481 275-292.

482 Sato, H., & Emoto, K. (2017). Synthesis of a scalar wavelet intensity propagating through von
483 Kármán-type random media: joint use of the radiative transfer equation with the Born approximation and
484 the Markov approximation. *Geophysical Journal International*, 211(1), 512-527.

485 Sato, H., Fehler, M. C., & Maeda, T. (2012). *Seismic wave propagation and scattering in the*
486 *heterogeneous earth*. Springer Science & Business Media. ISBN 978-3-642-23028-8.

487 Shapiro, S. A., & Kneib, G. (1993). Seismic attenuation by scattering: theory and numerical results.
488 *Geophysical Journal International*, 114(2), 373-391.

489 Vyas, J. C., Mai, P. M., Galis, M., Dunham, E. M., & Imperatori, W. (2018). Mach wave properties
490 in the presence of source and medium heterogeneity. *Geophysical Journal International*, 214(3), 2035-
491 2052. Yoshimoto, K., Takemura, S., & Kobayashi, M. (2015). Application of scattering theory to P-wave
492 amplitude fluctuations in the crust. *Earth, Planets and Space*, 67(1), 199.

493

494

495

496

497

498

499

500

501

502

503

504

505

506

507

508

509 **Author's full physical mailing addresses:**

510 Dr. Jagdish Chandra Vyas,
511 Building 1, Level 3, office #3110,
512 King Abdullah University of Science and Technology (KAUST),
513 Jeddah, Thuwal, 23955, Saudi Arabia.

514

515

516 Dr. Martin Galis,
517 Department of Astronomy, Physics of the Earth, and Meteorology,
518 Faculty of Mathematics, Physics and Informatics,
519 Comenius University,
520 Mlynska dolina F1,
521 842 48 Bratislava,
522 Slovakia.

523

524

525 Prof. Paul Martin Mai,
526 Building 1, Level 3, office #3114,
527 King Abdullah University of Science and Technology (KAUST),
528 Jeddah, Thuwal, 23955, Saudi Arabia.

529

530

531

532

533

534

535

536

537

538 **List of Table Captions**

539 **Table 1:** Parameters for the 28 computational 3D Earth models generated for this study.

540

541 **List of Figure Captions**

542 **Figure 1: (a,b):** S-wave speed distribution at the free surface for twelve 3D computational models for the
543 regime $k_w a \gg 1$, generated using three correlation lengths (1.0 km, 5.0 km, 10.0 km), two standard
544 deviations (5%, 10%) and two Hurst exponents (0.1, 0.5). The black star marks the epicenter. The sites
545 used for waveform comparison (black triangles, s1, s2, s3, s4, s5 and s6) and ground-motion analysis (black
546 dots in circular rings) are also shown. The beach ball shows the focal mechanism of the earthquake source.
547 Panels (a) and (b) depict random media with Hurst exponent 0.1 and 0.5, respectively. **(c):** Theoretical 1-
548 D power spectra (PSD) for 3D Earth structure for seven selected models. Correlation length and Hurst
549 exponent alter the shape of the power spectra (solid lines), whereas standard deviation only scales the
550 PSD (mark dashed line; notice the scaling of M4 compared to M1, but their identical shape). **(d):** The
551 theoretical power spectra of the random media are constrained by the dimensions of the computational
552 model and the spatial grid size. The dashed and solid lines are spectra related to models M2 and M11,
553 whereas three different colors depict power spectra sampled according to the three scattering regimes.

554

555 **Figure 2:** Horizontal components (East-West, EW, and North-South, NS) of ground acceleration (m/s^2) at
556 sites s1, s2, s3 (Fig 1a). Black dotted lines indicate theoretical P- and S-wave arrival times in the considered
557 homogeneous medium. Color-coded numbers indicate PGA values at individual sites. Waveforms are
558 normalized by their PGA-value in the homogeneous-medium simulations for a given site. (a) Illustration

559 of scattering controlled by σ for $k_w a \gg 1$ and small H ; (b) Illustration of negligible effects of correlation
560 length on scattering for $k_w a \gg 1$ and small H .

561

562 **Figure 3:** Mean PGA ratios (MPR) for all twelve numerical simulations as a function of distance, depicting
563 the effects of wavefield scattering on ground-motions in the regime $k_w a \gg 1$. Panels (a) and (b) depict
564 MPR for media with $H=0.1$ and $H=0.5$, respectively. Grey dashed lines are plotted to facilitate the MPR
565 comparison in two nearby panels. Wavefield scattering is proportional to the standard deviation of
566 medium heterogeneities, and inversely proportional to correlation length for large Hurst exponent ($H=$
567 0.5), but remains nearly unaffected by variations in correlation length for small Hurst exponent ($H= 0.1$).
568 The $k_w a$ maxima for correlation lengths of 1, 5 and 10 km are 9.07, 45.36 and 90.72, respectively.

569

570 **Figure 4:** Mean PGA ratios (MPR) for eight numerical simulations as a function of distance, depicting the
571 effects of wavefield scattering on ground-motions in the regime $k_w a \approx 1$. Panels (a) and (b) depict MPR
572 for media with $H=0.1$ and $H=0.5$, respectively. Grey dashed lines are plotted to facilitate the MPR
573 comparison in two nearby panels. Wavefield scattering is proportional to correlation length, Hurst
574 exponent, and standard deviation of medium heterogeneities. The highest values of $k_w a$ for correlation
575 lengths of 1 and 5 km are 0.90 and 4.53, respectively.

576

577 **Figure 5:** Mean PGA ratios (MPR) for all eight numerical simulations as a function of distance, depicting
578 the effects of wavefield scattering on ground-motions in the regime $k_w a \ll 1$. Panels (a) and (b) depict
579 MPR for media with $H=0.1$ and $H=0.5$, respectively. Grey dashed lines are plotted to facilitate the MPR
580 comparison in two nearby panels. Wavefield scattering is proportional to correlation length, Hurst

581 exponent, and the standard deviation of medium heterogeneities. The highest values of $k_w a$ for
582 correlation lengths of 5 and 10 km are 0.27 and 0.54, respectively.

List of Tables

Table 1: Parameters for the 28 computational 3D Earth models generated for this study.			
Model Reference	Correlation length a (km)	Standard deviation σ (%)	Hurst exponent H
M1, M1-L	1.0	5	0.1
M2, M2-L, M2-EL	5.0	5	0.1
M3, M3-EL	10.0	5	0.1
M4, M4-L	1.0	10	0.1
M5, M5-L, M5-EL	5.0	10	0.1
M6, M6-EL	10.0	10	0.1
M7, M7-L	1.0	5	0.5
M8, M8-L, M8-EL	5.0	5	0.5
M9, M9-EL	10.0	5	0.5
M10, M10-L	1.0	10	0.5
M11, M11-L, M11-EL	5.0	10	0.5
M12, M12-EL	10.0	10	0.5

Parameters of 28 computational 3D models generated using random fields characterized by von Karman autocorrelation functions (parametrized by correlation length, standard deviation and Hurst exponent). The suffixes “-L” and “-EL” indicate large and extra-large models, respectively.

List of Figures

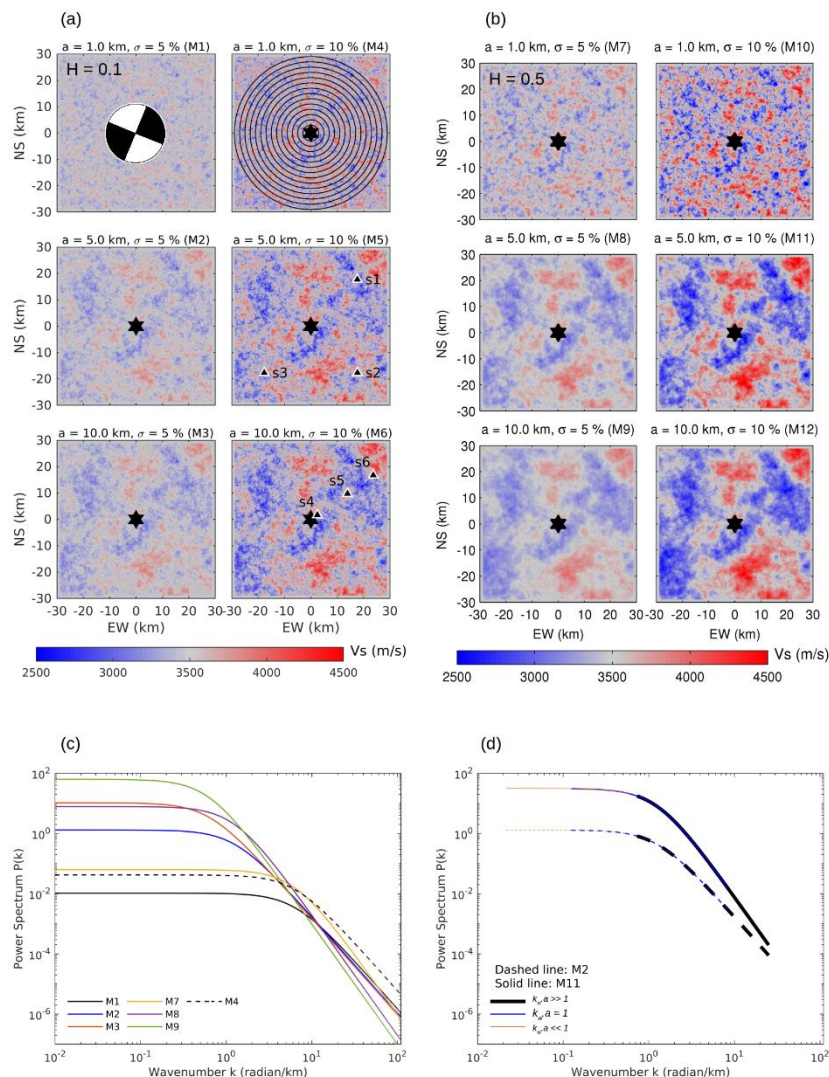


Figure 1: (a,b): S-wave speed distribution at the free surface for twelve 3D computational models for the regime $k_w a \gg 1$, generated using three correlation lengths (1.0 km, 5.0 km, 10.0 km), two standard deviations (5%, 10%) and two Hurst exponents (0.1, 0.5). The black star marks the epicenter. The sites used for waveform comparison (black triangles, s1, s2, s3, s4, s5 and s6) and ground-motion analysis (black dots in circular rings) are also shown. The beach ball shows the focal mechanism of the earthquake source. Panels (a) and (b) depict random media with Hurst exponent 0.1 and 0.5, respectively. **(c):** Theoretical 1-D power spectra (PSD) for 3D Earth structure for seven selected models. Correlation length and Hurst exponent alter the shape of the power spectra (solid lines), whereas standard deviation only scales the PSD (mark dashed line; notice the scaling of M4 compared to M1, but their identical shape). **(d):** The theoretical power spectra of the random media are constrained by the dimensions of the computational model and the spatial grid size. The dashed and solid lines are spectra related to models M2 and M11, whereas three different colors depict power spectra sampled according to the three scattering regimes.

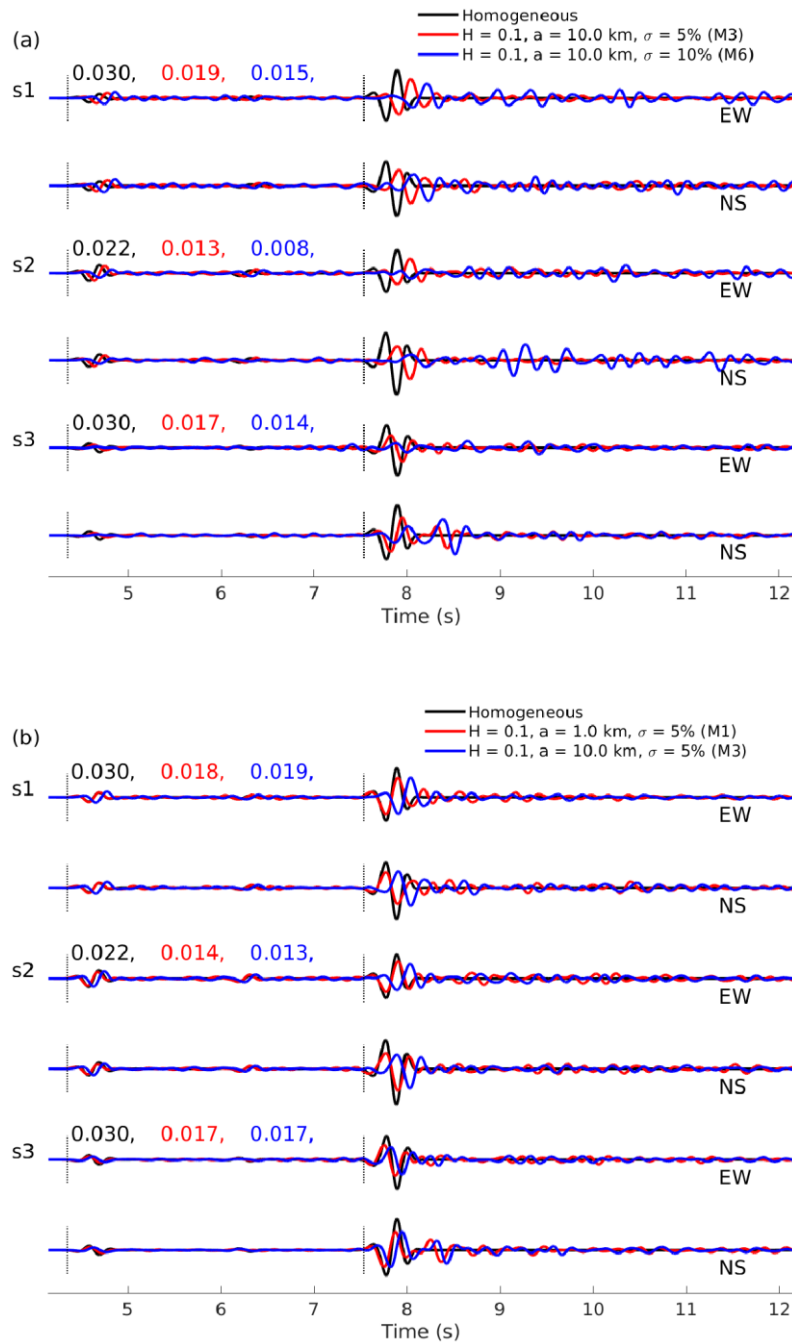


Figure 2: Horizontal components (East-West, EW, and North-South, NS) of ground acceleration (m/s^2) at sites s1, s2, s3 (Fig 1a). Black dotted lines indicate theoretical P- and S-wave arrival times in the considered homogeneous medium. Color-coded numbers indicate PGA values at individual sites. Waveforms are normalized by their PGA-value in the homogeneous-medium simulations for a given site. (a) Illustration of scattering controlled by σ for $k_w a \gg 1$ and small H ; (b) Illustration of negligible effects of correlation length on scattering for $k_w a \gg 1$ and small H .

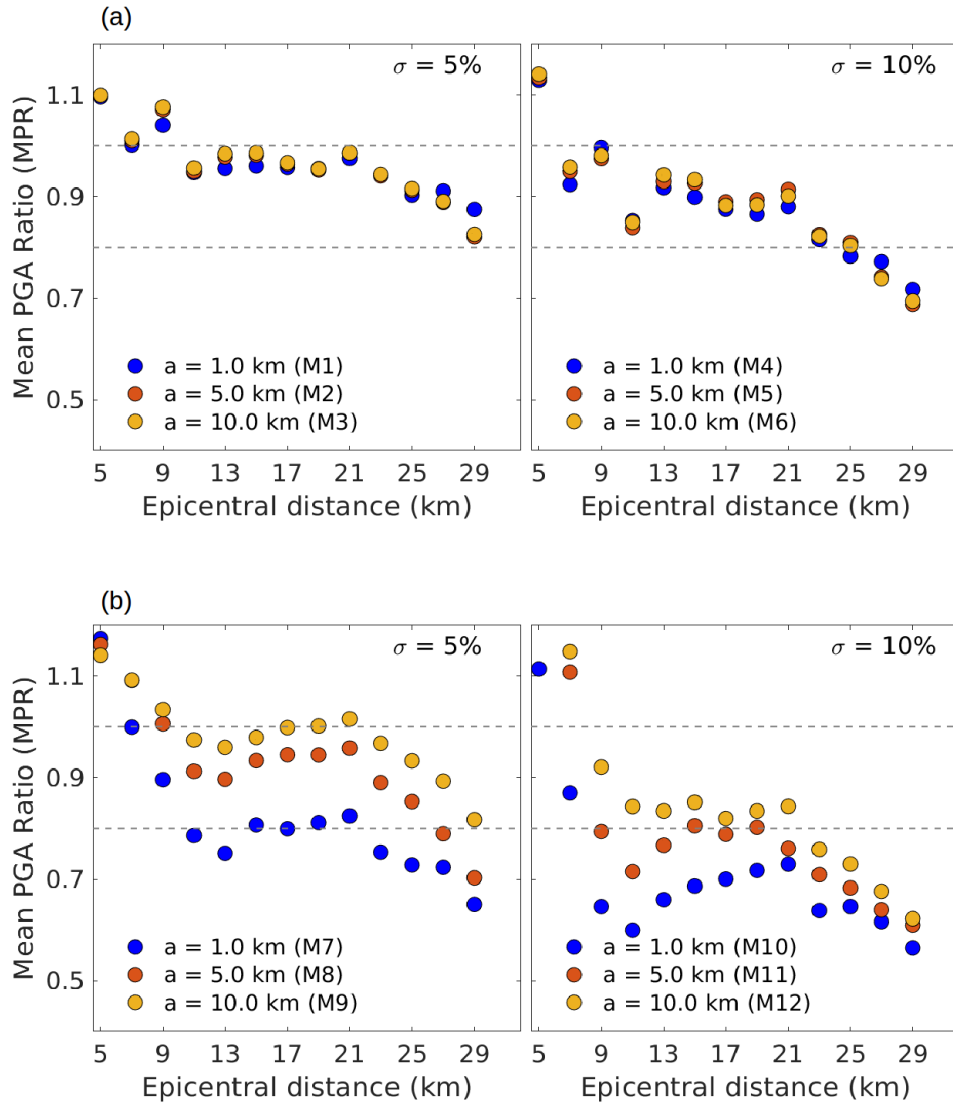


Figure 3: Mean PGA ratios (MPR) for all twelve numerical simulations as a function of distance, depicting the effects of wavefield scattering on ground-motions in the regime $k_w a \gg 1$. Panels (a) and (b) depict MPR for media with $H=0.1$ and $H=0.5$, respectively. Grey dashed lines are plotted to facilitate the MPR comparison in two nearby panels. Wavefield scattering is proportional to the standard deviation of medium heterogeneities, and inversely proportional to correlation length for large Hurst exponent ($H=0.5$), but remains nearly unaffected by variations in correlation length for small Hurst exponent ($H=0.1$). The $k_w a$ maxima for correlation lengths of 1, 5 and 10 km are 9.07, 45.36 and 90.72, respectively.

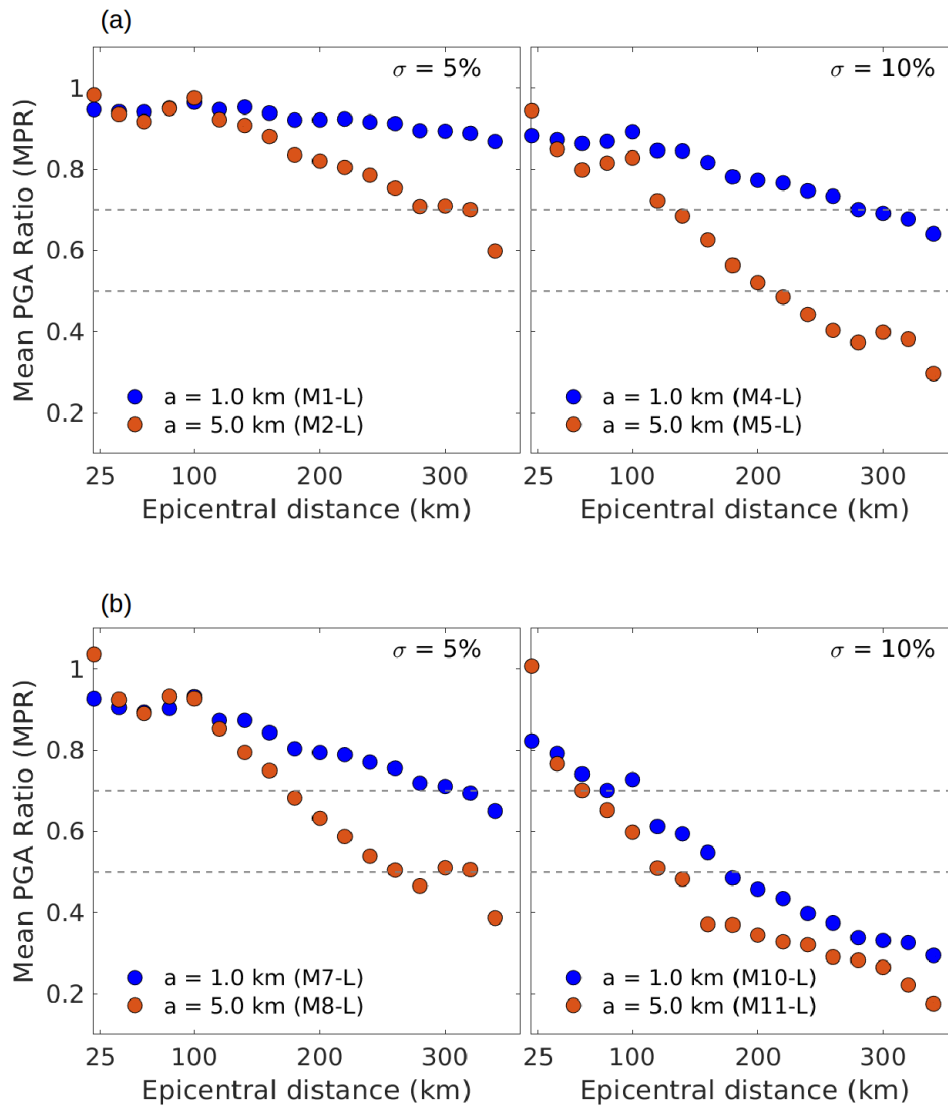


Figure 4: Mean PGA ratios (MPR) for eight numerical simulations as a function of distance, depicting the effects of wavefield scattering on ground-motions in the regime $k_w a \approx 1$. Panels (a) and (b) depict MPR for media with $H=0.1$ and $H=0.5$, respectively. Grey dashed lines are plotted to facilitate the MPR comparison in two nearby panels. Wavefield scattering is proportional to correlation length, Hurst exponent, and standard deviation of medium heterogeneities. The highest values of $k_w a$ for correlation lengths of 1 and 5 km are 0.90 and 4.53, respectively.

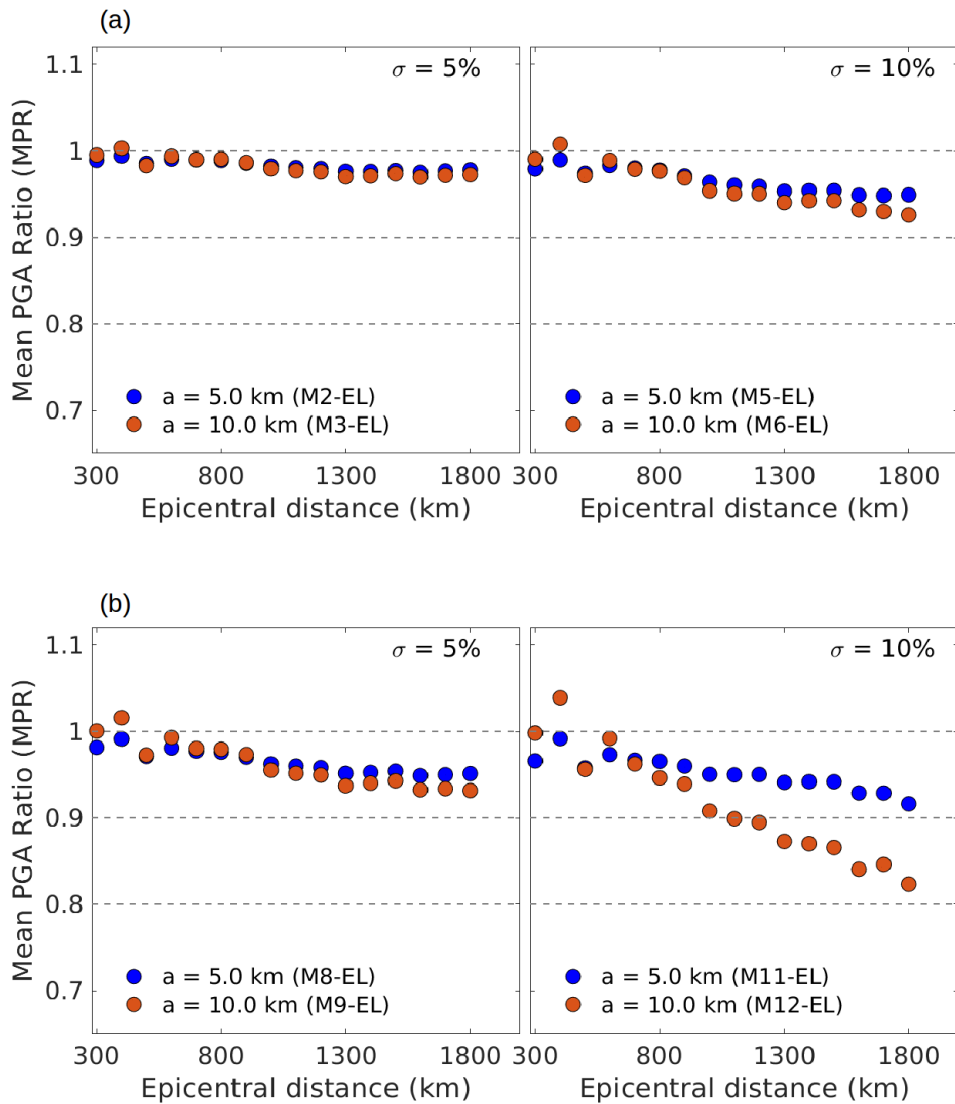


Figure 5: Mean PGA ratios (MPR) for all eight numerical simulations as a function of distance, depicting the effects of wavefield scattering on ground-motions in the regime $k_w a \ll 1$. Panels (a) and (b) depict MPR for media with $H=0.1$ and $H=0.5$, respectively. Grey dashed lines are plotted to facilitate the MPR comparison in two nearby panels. Wavefield scattering is proportional to correlation length, Hurst exponent, and the standard deviation of medium heterogeneities. The highest values of $k_w a$ for correlation lengths of 5 and 10 km are 0.27 and 0.54, respectively.